

Detection of Hydromorphologic Characteristics of Indus River Estuary, Pakistan, Using Satellite and Field Data

Muhammad Wajid Ijaz^{1,2} · Altaf Ali Siyal^{1,3} · Rasool Bux Mahar¹ · Waqas Ahmed¹ · Muhammad Naveed Anjum⁴

Received: 16 November 2016 / Accepted: 10 April 2017
© King Fahd University of Petroleum & Minerals 2017

Abstract Natural and anthropogenic factors directly determine the hydromorphologic and ecologic equilibrium of riverine environment. The present study was designed to detect the hydromorphologic characteristics of Indus River Estuary (IRE) using medium and high spatial resolution multispectral satellite imagery along with field data. Qualitative (visual) and quantitative (analytical) analysis was undertaken, and accuracy of each method as well as remotely sensed data was assessed. Single-band density slicing method was used for water bodies, while multiband supervised and unsupervised classification methods were adopted for the identification of hydromorphologic habitat along with key ecologic features of the IRE. The analysis of satellite imagery

showed that the shortwave infrared-2 (band 7) of Landsat-8 Operational Land Imager (OLI) sensor performed better than its visible bands for delineating water bodies. The overall classification accuracy was 89%. Supervised classification with the maximum likelihood algorithm performed better for OLI imagery (30 m) than high spatial resolution RapidEye (5 m) imagery. However, unsupervised classification method was not suitable due to the significant overlapping of inter- and intra-class pixels. Overall, due to its adequate spectral range Landsat OLI imagery was utilized for monitoring of terrestrial water bodies and their morphologic features. Thus, we recommend that selecting the spatial resolution of the imagery should be based on the size of the objects to be recognized.

✉ Muhammad Wajid Ijaz
wajidijaz331@gmail.com

Altaf Ali Siyal
aasiyal.uspcasw@faculty.muett.edu.pk

Rasool Bux Mahar
rb.mahar@faculty.muett.edu.pk

Waqas Ahmed
wapathan.uspcasw@faculty.muett.edu.pk

Muhammad Naveed Anjum
naveedwre@lzb.ac.cn

¹ U.S.-Pakistan Centre for Advanced Studies in Water, Mehran University of Engineering and Technology, Jamshoro, Sindh 76062, Pakistan

² Environmental Protection Agency, Lahore, Punjab 54000, Pakistan

³ Department of Land and Water Management, Sindh Agriculture University, Tandojam, Sindh 70060, Pakistan

⁴ Division of Hydrology Water-Land Resources in Cold and Arid Regions, Cold and Arid Regions Environmental and Engineering Research Institute, Chinese Academy of Sciences, Lanzhou 730000, People's Republic of China

Keywords Water bodies · Classification · River Indus · Density slicing

1 Introduction

The regulation of river flow and rapidly changing land use–land cover are major determinants to the ecological health of floodplains [1]. The agricultural productivity of river floodplains is well established all over the world, but contemporary climate change-induced hydrometeorological extremes are exceeding previous hydrological and morphological anomalies. River features are a function of hydrodynamic activities those potentially trigger the avulsion processes [2]. Regular monitoring plays an important role for the sustainable management of natural resources, but it is constrained by available time, financial and human resources for land surveys. The advancement of remote sensing and geographic information system (GIS) technologies has helped to address these obstacles [3–6]. Imaging

of the land surface with passive sensors allows the detection and discrimination of ground objects based on their molecular composition and geometrical shapes using multispectral (red, green, blue) and panchromatic (grayscale) data. The spectral resolution has been extended with near-infrared (NIR) and shortwave-infrared (SWIR) bands up to the hyperspectral range. Landforms can be detected in remotely sensed imagery and linked to ground measurements for interpretation using a broad range of spectral signatures [7,8]. Water detection techniques have been categorized into four major categories, namely statistical patterns based on supervised and unsupervised image classification, linear unmixing, single-band thresholding and spectral indices [9]. Various studies have used density slicing for the discrimination of water bodies from remotely sensed imagery [10,11].

Gilvear et al. [12] characterized the morphological landforms of River Tummel, Scotland, using supervised and unsupervised classification techniques and high spatial resolution imagery (<2 m) for a 50-m-wide channel. Isikdogan et al. [14] used the Normalized Difference Water Index (NDWI) for the separation of water and background features using Landsat-8 imagery over Yangtze and Huaihe river basins in China. The authors determined thresholds for each model at an overall accuracy of 95% using the Otsu method. Similarly, [14] separated water and non-water pixels using NDWI calculated from Landsat-8 imagery and subsequently extracting the river network through the modified multiscale singularity index for the estimation of the river centerline and channel width. In a recent study, [15] achieved an overall agreement of 30% between water bodies over the plane and hilly Murray–Darling basin, Australia, using Landsat-8 imagery and Open Street Maps in conjunction with SRTM 30-m elevation data.

Khan et al. [16] used satellite imagery for the visual interpretation of shoreline change along the coast of Sindh. Siddiqui et al. [17] studied the spatial and temporal change in floodplains and riverine forests in Sindh using Landsat-5 and Landsat-7 imagery. Qamer et al. [18] characterized the wetlands in Pakistan using object-based image analysis and 0.6-m high-resolution satellite imagery. A detailed study by [19] traced floodplain changes corresponding to floods and their subsequent river meandering in lowlands of the world rivers including the Indus River using multiresolution imagery. Mahar and Zaigham [20] determined the impact of anthropogenic effects over the widening of the lower section of the Indus River using Landsat imagery. A comprehensive account of mangrove habitat along the coastlines of Pakistan, India, Bangladesh and Sri Lanka was made using supervised and unsupervised classification methods over Landsat ETM+ imagery [9]. These studies indicate that Landsat imagery has been used for individual aims like vegetation detection and floodplain tracking. The present study assesses the usefulness of Landsat-8 OLI imagery and determines more suitable methods for water body detection.

Furthermore, comprehensive hydromorphologic characteristics of the estuarine section of the Indus River in the lowlands of Pakistan are characterized with small field data in conjunction with high spatial resolution imagery from the RapidEye sensor.

Gilvear et al. [21] argue that riverine environments can be completely delineated and spatiotemporal changes quantified by using multispectral remotely sensed imagery. Thus, the overall purpose of this study is to evaluate: (1) the suitability of single band and multispectral band(s) of the OLI sensor of Landsat-8 for water bodies detection and (2) the extraction accuracy of river morphologic features and identification of best-fit classification technique using an error matrix. Ultimately, the present study will contribute to ongoing attempts for the consolidation of techniques for turning imagery into information and to the development of a more comprehensive algorithm for the semi-automatic or automatic recognition of river morphodynamics and subsequent thematic landform changes.

2 Materials and Methods

2.1 Study Area

The study area is located in the terminal section of the River Indus in Sindh Province of Pakistan. The section is about 110 km downstream of Kotri Barrage, which spreads over 150 km in length and 0.2–1 km in width across the river course. It traverses the Indus delta starting from Sujawal bridge (Fig. 1), and after observing high sinuosity its mouth opens into the Arabian Sea near Keti Bandar. An interesting fact pertaining to the site selection lies in its diversified hydraulic, geomorphologic and ecologic habitat. The river flows of this section are a prime source of freshwater to estuary as it receives very low rainfall of 150–200 mm annually. The tides along the coast of Karachi are semi-diurnal with two highs and two lows every day but vary significantly from each other in tidal heights during the daily tidal cycle [22]. Due to the intrusion of highly saline seawater, water quality in this deltaic plain has been degraded and groundwater is more or less considered as brackish.

The average annual flow of water downstream of Kotri Barrage is approximately 180 billion m³, and the sediment flux is 400 million tons. Ecological stresses are increasing due to the weakening of fluvial controls and the loss of physical habitat in the result of strong tidal activities.²⁰ During summer, intense monsoon winds from the southwest cause parts of the delta to be intruded by seawater. During the winter, the winds in this area blow from the northeast side. Relic channels, wide floodplains confined within levees, river meandering, oxbow lakes and sand bars constitute the hydromorphologic habitat of this site. Geologically, the area is

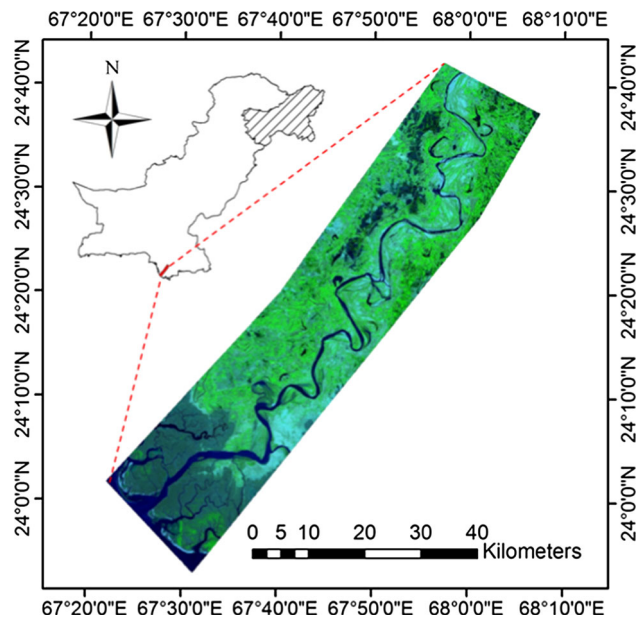


Fig. 1 Location of estuarine section of the Indus River in Sindh, Pakistan

considered as a configuration of alluvial deposits, mainly supporting the production of wheat, rice and sugarcane crops.

2.2 Remotely Sensed Dataset and Preprocessing

Landsat-8 imagery with path 152 and row 43 was acquired from USGS earth explorer (<http://earthexplorer.usgs.gov>). Composite images in three colors (red, green, blue) were individually made by stacking five bands of RapidEye and the first seven bands of Landsat-8 OLI sensor, respectively. Panchromatic band 8 of OLI was used to sharp the OLI image as suggested by researchers and spatial resolution of the composite image of Landsat-8 was increased from 30 to 15 m [15]. No radiometric correction was applied because 3A product of RapidEye sensor used in this study was already ortho-rectified and radiometrically corrected (Fig. 2).

As the water level of water bodies keeps changing under prevailing hydrometeorological conditions, it is hard to undertake accurate ground-truthing for verification of spatial extent of the water surface [23]. Therefore, a high spatial resolution image of the RapidEye sensor (5 m) along with Google Earth was used as primary and secondary references, respectively, for visual interpretation of results of automatic classification process [13,24–27].

2.3 Image Processing and Analysis

Composite images were classified using ArcMap software as follows:

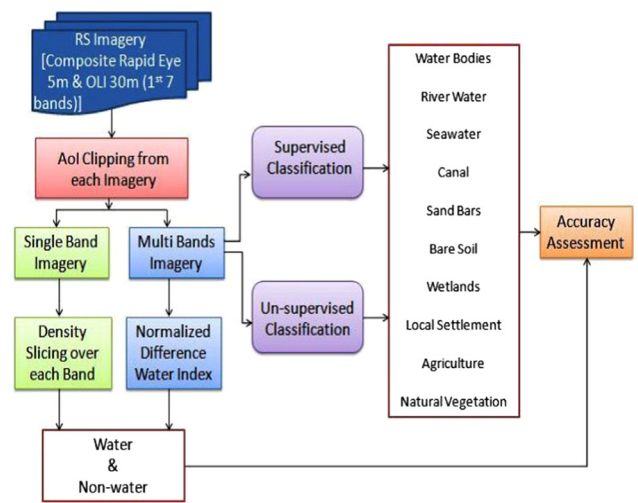


Fig. 2 Workflow diagram for detection of water bodies and delineation of hydromorphologic features of study area

Single-band density slicing bifurcates the image into targeted and background featured class, e.g., in this study water and non-water, which enables to classify each pixel based on their spectral signature. Appropriate sample size and sampling scheme lead to a more accurate result of the separation technique. In this study, the sampling size of ground-truthing points for density slicing was 160 and was decided based on binomial probability theory.

The maximum likelihood algorithm was used for the supervised classification and ISO-cluster algorithm for the unsupervised classification using ArcMap 10.3.1. For the supervised classification, the training areas of 11 classes (water bodies, river water, seawater, canal, sand bars, bare soil, wet soil, levees, local settlement, agriculture and natural vegetation) were chosen through visual interpretation of high-resolution imagery and Google Earth as true representation of the targeted class on the ground as described in Table 2. Meanwhile, a stratified random sampling scheme was exercised for picking up those training sites. Training areas in density slicing of single band were established as point and multiple polygons for each class in supervised classification.

The location of the training samples was the same for all images. The spectral signature for each training site was derived individually for the supervised classification of each image. Furthermore, each image was segmented into 55 classes using unsupervised classification. Each class was inspected visually and was grouped into 10 main land cover classes, namely water bodies combining oxbow lakes and lagoons, river water, seawater, canal, sand bars, bare soil, wet soil, local settlements combining digital signature of levees, agriculture and natural vegetation. The area occupied by each class in all images was calculated with their bounding polygons in the respective shape file.

The classification accuracy depends considerably on the quality and accuracy of the training data. Errors in the training

Table 1 Summary of spatial and spectral resolution of satellite imagery used in the study

Dataset	Type	Spectral resolution (nm)	Spatial resolution (m)	
Landsat-8 OLI (single tile, acquisition date 10-17-2014)	Multispectral imagery with visible, infrared, panchromatic and thermal bands having radiometric resolution of 16 bits, cloud cover = 0.85	Band 1 (Coastal Aerosol)	430–450	30
		Band 2 (Blue)	450–510	30
		Band 3 (Green)	530–590	30
		Band 4 (Red)	640–670	30
		Band 5 (NIR)	850–880	30
		Band 6 (SWIR1)	1570–1650	30
		Band 7 (SWIR2)	2110–2290	30
		Band 8 (Panchromatic)	500–680	15
RapidEye (8 tiles, acquisition date 10-28-2014)	Multispectral 3A ortho-product with radiometric, sensor and geometric corrections, cloud cover = 0	Band 1 (Blue)	440–510	5
		Band 2 (Green)	520–590	5
		Band 3 (Red)	630–685	5
		Band 4 (Red Edge)	690–730	5
		Band 5 (NIR)	760–850	5

Table 2 Description of targeted classes

Superclass	Class	Characteristics
Water	Water bodies	Oxbow lakes, lagoons, relic channel having stagnant water
	River	Open water stream having freshwater
	Seawater	Oceanic portion having brackish water
	Canal	Open water stream having freshwater
Land	Sand bars	Dry sand deposited during sediment transport
	Bare soil	Barren or open land without consumptive use
	Levee	Earthen embankment for flood protection
	Wetland/soil	Moist/saturated soil located in low-lying area
Vegetation	Local settlement	Particularly dense urban or rural build-ups/homestead, also includes masonry works and roads
	Natural vegetation	Area under dense/scattered forest/grass/shrubs, etc.
	Agriculture	Area under cultivation of crops

data can be due to errors in geometric calculations, unseparated land cover classes and incorrect labeling of training samples [28]. Therefore, the accuracy of each classification method was determined by selecting reference points using a stratified random scheme over the high spatial resolution (5m) image with the aid of Google Earth. ArcMap software compares the classified data with reference data and subsequently builds a confusion/error matrix. The correct-

ness of actual class is measured with producers' accuracy. Cohen's kappa coefficient, K , is a discrete multivariate technique that reflects the difference between actual agreement and the agreement expected by chance.

More generally accepted statistical and analytical techniques were used over actual and reference data for calculation of producers' accuracy, users' accuracy, commission and omission error [11,29]. Water area calculated with density slicing of each band was compared with water area extracted using Modified Normalized Difference Water Index (MNDWI), that is:

$$\text{MNDWI} = (\rho_{\text{green}} - \rho_{\text{SWIR1}}) / (\rho_{\text{green}} + \rho_{\text{SWIR1}})$$

where ρ_{green} and ρ_{SWIR1} are top of atmospheric (TOA) reflectance of band 3 and band 6, respectively, of Landsat-8 imagery.

Two ground-truthing visits were conducted in 2015 and 2016 during which permanent ground features were inspected, in particular the Sujawal bridge, some lengths of right and left bank levees, a distinguished island near the mouth of the river, scattered chunks of mangrove/natural vegetation in floodplains and local settlement. Handheld GARMIN's GPSMAP-64 device was used for the acquisition of georeferenced coordinates over RapidEye fine-resolution image of 2014.

3 Results and Discussion

3.1 Single-Band Density Slicing

Table 3 shows the spatial variation in mean pixel values of water bodies existing in the floodplain. The spectral variation of the water class in each spectral band could be attributed to

Table 3 Mean pixel values of water bodies in each band of OLI imagery

Training site	Mean pixel value						
	Band 1	Band 2	Band 3	Band 4	Band 5	Band 6	Band 7
Oxbow 1	10388.40	9541.80	8663.60	7844.20	9345.00	7441.20	6492.40
Oxbow 2	10395.00	9681.40	9209.40	8327.40	7602.60	6689.20	6205.20
Oxbow 3	10646.80	10039.80	9772.60	8768.00	7408.60	6438.80	6006.80
Oxbow 4	10534.40	9826.00	9406.00	8209.60	7308.00	6446.00	6040.80
Oxbow 5	10625.20	10034.80	9803.60	8312.20	7061.00	6205.60	5845.80
Oxbow 6	10511.40	9818.40	9422.60	8292.80	7313.40	6473.40	6050.00
River	10846.33	10302.56	10153.33	8862.44	7415.00	6581.00	6174.67
Seawater	10869.60	10283.80	9782.80	8436.40	6506.60	5808.20	5605.40
Lagoon 1	10446.67	9772.67	9467.00	8308.33	7217.67	6271.67	5865.00
Lagoon 2	10549.67	9906.00	9557.33	8611.67	7299.67	6459.33	6049.00
Lagoon 3	10342.00	9668.00	9238.67	8076.67	7233.67	6298.33	5903.33
Lagoon 4	10317.67	9565.67	8969.34	8280.00	7079.00	6192.33	5833.33
Lagoon 5	10426.67	9656.67	9233.67	8352.67	7405.33	6518.00	6072.67
Lagoon 6	10168.00	9271.00	8319.67	7725.33	7246.33	6286.67	5878.33
St. deviation	197.84	290.88	499.17	336.53	287.79	223.67	158.94

Table 4 Distribution of water class digital numbers among each band of OLI imagery

Band	Spectral wavelength (μm)	Band range		Water range	
		Minimum	Maximum	Minimum	Maximum
1	0.43–0.45	9952	15,291	10,138	11,270
2	0.45–0.51	9040	15,573	9223	10,858
3	0.53–0.59	7913	17,152	8253	10,827
4	0.64–0.67	7240	20,212	7542	9779
5	0.85–0.88	6196	24,422	6371	8500
6	1.57–1.65	5575	41,835	5720	7252
7	2.11–2.29	5424	59,162	5525	6612

different reflective responses of each water body. The standard deviation of the water class started declining as the spectral wavelength crossed 600nm and catches its lowest value in the shortwave infrared-2 (band 7) of OLI imagery.

Similarly, pixel range of water bodies also started squeezing from the 4th band and observed the lowest range in the 7th band as presented in Table 4.

Separation results of density slicing of each band are shown in Fig. 3. Visual inspection of these results shows that the first four bands in the visible range overestimated water areas, probably due to the overlapping of the large spectral range of water class pixels with adjacent vegetation and bare soil area pixels.

Single band of OLI sensor of Landsat-8: (A) band 1, (B) band 2, (C) band 3, (D) band 4, (E) band 5, (F) band 6, (G) band 7 and (H) MNDWI_{6,3}. Oxbow lakes, lagoons, river reach and tidal channels were separated distinctly in the infrared range with bands 5, 6 and 7, respectively. However, quantitative measures of all bands were compared with Modified Normalized Difference Water Index, which was

calculated using bands 6 and 3 [13]. The cumulative results of the water class in the visible range were very high, while IR bands yielded low as shown in Fig. 4. A detailed inspection of the results revealed that three bands of the IR range misinterpreted the reflectance of tidal waves in principle and translated those pixels as non-water class. Similarly, tidal creeks of the coastal belt having a maximum width of <50m and canals in the upper region having a maximum width of less than the size of a pixel could not be separated adequately and were incorrectly attributed to the non-water class. That is why the area classified as water was lesser and non-water was consequently higher than that of the Modified Normalized Difference Water Index in Fig. 4 [13].

Results given in Table 5 are substantiating the aforementioned findings of visual interpretation. The commission error of the water class is highest in the first three bands (1, 2, 3) and as low as zero in the last three bands (5, 6, 7). The reason behind the overestimation of the water class was the stretched DN range of the visible bands (Table 4), and it led to a poor separation and automatic account of mixed pixels of vegeta-

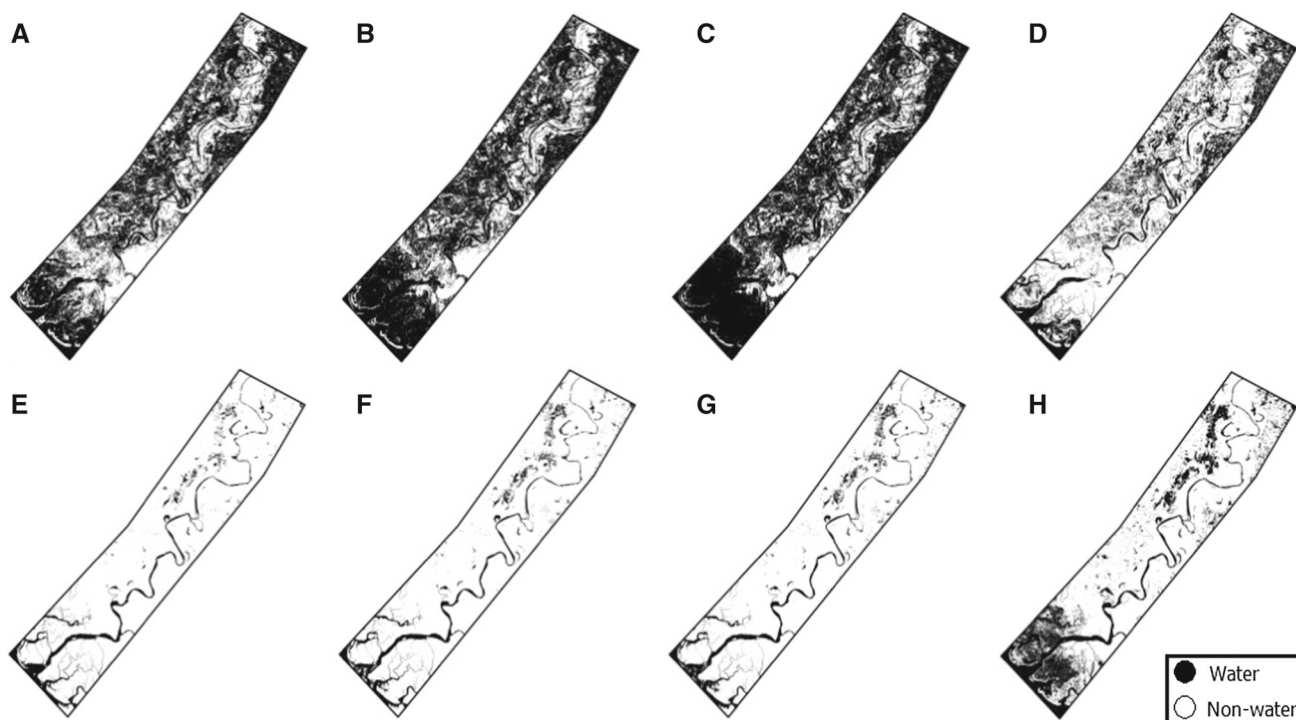


Fig. 3 Density slicing for image segmentation into two major classes, water and non-water

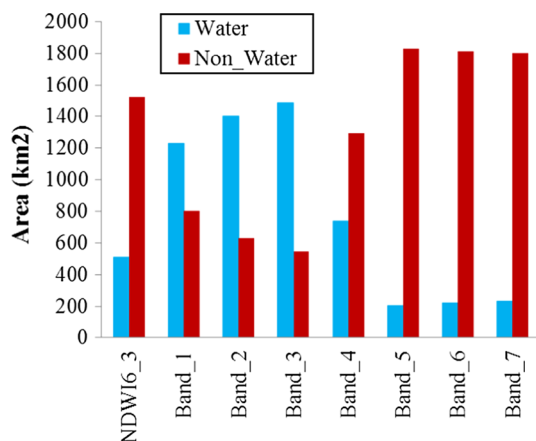


Fig. 4 Water and non-water area in km² depicting close suitability of near-infrared (NIR) to shortwave-infrared (SWIR1 & SWIR2) bands 5–7

tion, bare soil and other classes as the water class. Moreover, clips of the first seven bands shown in Fig. 5 are showing that pixel-count histograms in the visible range are unimodal and histograms of the infrared range are multimodal. The DN distribution along the x-axis of bands 1, 2, 3 and 4 (shown in red) is more than the remaining bands, which is why the overlapping of mixed pixels with the water class resulted in an overestimation [11]. Distinguished peaks and multimodal attributes of the IR bands are adequately useful for multiclass separation with a single band.

Similarly, at 100% water class users' accuracy was also verified through overall classification accuracy and kappa coefficient of 89.38% and 0.78 for bands 5 and 7, respectively. Therefore, selection of a more suitable band for water bodies detection was difficult because of the similarity of results between band 5 and band 7.

The performance depicted in Fig. 4 in comparison with NDWI shows that the water class areas obtained from band 7 were somewhat better, as 229 km² than band 5 which is determined as 201 km². Likewise, the pixel range for a variety of water bodies as shown in Table 4 is also confirming the suitability of band 7 with the lowest pixel range of 1087, whereas this range for band 5 is 2129. With highest classification accuracy, good water body area estimation, smallest pixel range under one peak of multimodal histogram and lowest corresponding errors, band 7 has offset the remaining first six bands of OLI sensor of Landsat-8 as also demonstrated by (42) and has proven as more suitable single discriminating band for detection of variety of water bodies present in this estuarine section and adjoining coastal zone of Pakistan [41].

3.2 Multiband Classification

3.2.1 Visual Assessment

A composite color image was produced by displaying 5 bands of high-resolution RapidEye imagery at a scale of 1:12,500. In the color image, the majority of hydromorpho-

Table 5 Breakdown of density slicing classification using error matrix

Band	Confusion matrix		Overall classification accuracy	Kappa coefficient, K	Water class commission error	Water class omission error	Water class producer's accuracy	Water class user's accuracy
	Class	Class						
1	Water	79	75.63	0.51	31.86	0.033	96.25	68.14
	Non-water	1						
2	Water	79	76.25	0.52	31.90	0.011	98.75	68.10
	Non-water	1						
3	Water	76	71.88	0.43	35.04	0.043	95.00	64.96
	Non-water	4						
4	Water	63	75.00	0.50	26.75	0.250	78.75	73.26
	Non-water	17						
5	Water	63	89.38	0.78	0	0.340	78.75	100.0
	Non-water	17						
6	Water	62	88.75	0.77	0	0.363	77.50	100.0
	Non-water	18						
7	Water	63	89.38	0.78	0	0.340	78.75	100.0
	Non-water	17						
MNDWI	Water	79	91.25	0.82	14.13	0.014	98.75	85.87
	Non-water	1						



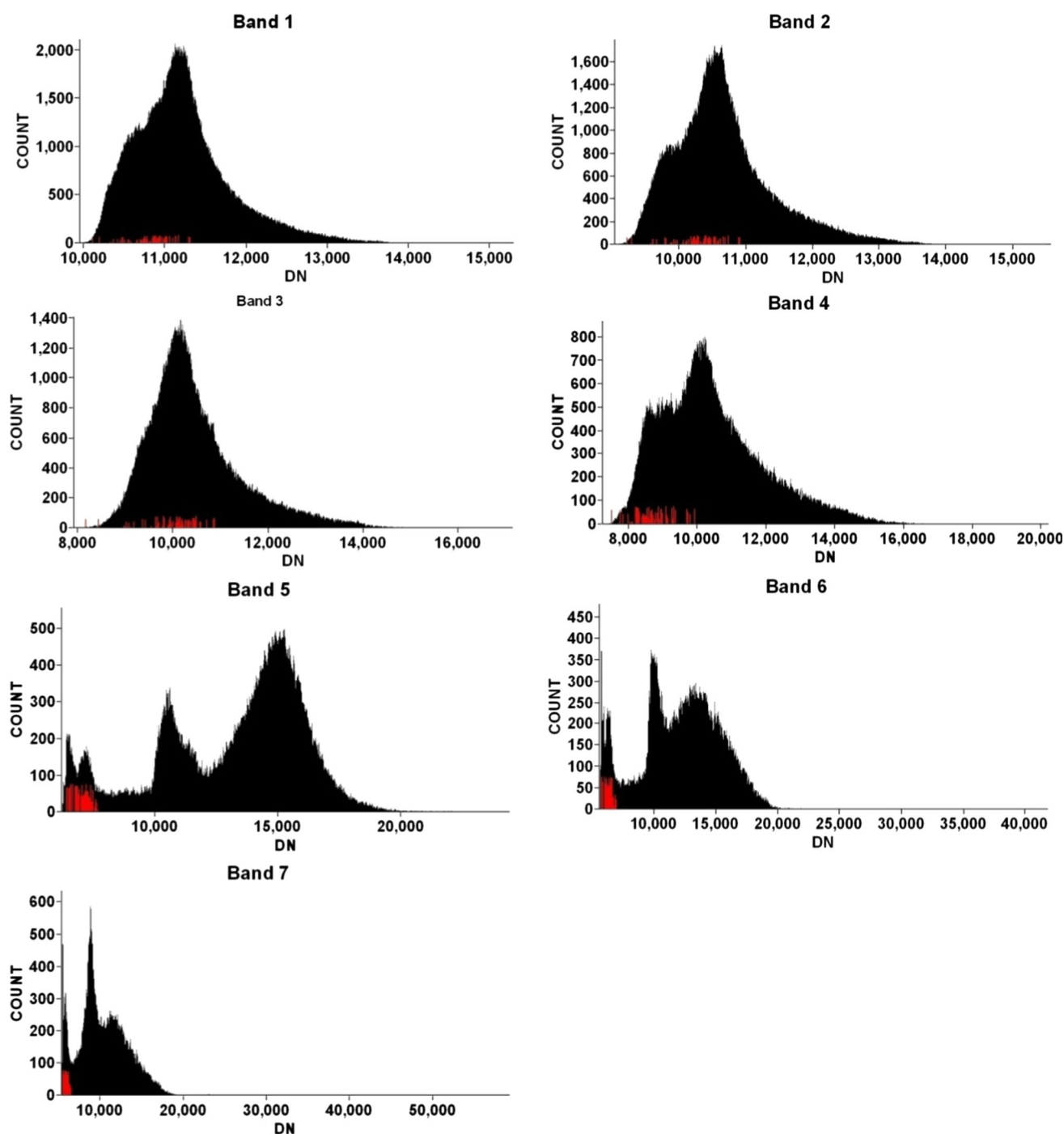


Fig. 5 Individual histograms (black color) of the first seven bands of OLI imagery with water training pixels (red color)

logic features in the floodplain and man-made land uses were detectable as shown in Figs. 9 and 10. All water bodies (lagoons, oxbow lakes, and ponds detected with single-band density slicing) were apparent with well-defined boundaries. Besides major stream channels with wide top-width of >500m and major creeks of >200m, the channels and relic channels with short top-width of <40m, tidal channels <10m, wastewater drain <15 m were easily identifiable.

Sand dunes and point bars deposited near meandering bends and bare soil in the floodplain were also distinguishable without any image enhancement. Agricultural fields were visible, but the sparse vegetation was a bit hard to identify. Google Earth was quite helpful for the differentiation of natural vegetation, in particular trees and shrubs. Roads, local settlements in the surrounding villages and towns along with patches of bare soil were visualized without difficulty.



Fig. 6 Visual comparison of spatial resolution using **a** Landsat color composite image of 30 m, **b** panchromatic band of OLI sensor of 15 m and **c** RapidEye color image of 5 m

The color imagery of the Landsat OLI sensor with a medium spatial resolution of 30 m at the same scale was only useful for identifying major streams such as river, creeks and relic channels. Water bodies like oxbow lakes, lagoons and other water ponds were easily recognizable, but it was very difficult to identify mixed pixels representing bare ground and wetlands. Local settlements and roads were overlapping with levee class pixels. Island and sand bars were easily detected with this image.

The visual effect of pan-sharpening of a color composite image with band 8 of the OLI sensor was observed, as shown in Fig. 6. Many of the features turned visible and corners of larger land cover classes were sharper. Major roads, levees and clusters of local settlements were distinguished at 15 m resolution. Water channels with top-width of 12 m and above got easy recognition, but the issue of mixed pixels of bare land with adjacent wet soil and local settlements was persisting. Only RapidEye image was able to detect the presence of tidal wave propagating landwards near the mouth of the river.

3.2.2 Unsupervised Classification

The level of agreement between the classified image and the real world is depicted with the help of an error matrix given in Table 6, 7 and 8. The overall classification for high spatial resolution imagery of RapidEye, medium-resolution Landsat-8 and the pan-sharpened imagery was 57.0, 54.9 and 55.4% and the commission error up to 54.6, 74.3 and 72.5%, respectively. Apparently, there exists a poor discrimination and notable overlapping between major classes like water, soil and vegetative landscapes.

A breakdown of misclassified pixels in the error matrix (Table 6) for high-resolution imagery is depicting that unsupervised classification could not perform better in intra-class cases. The majority of pixels of bare soil were overlapping with local settlements, by the reason their producers' accu-

racies were 23.5 and 35.1%, respectively, as shown in Fig. 7. Similarly, seawater was separated at 100% producer's accuracy with zero commission and omission error. But its user's accuracy was lower as 35.3% because fairly large proportions of river pixels and water bodies were incorrectly falling into the seawater class. The issue was verified through an analysis of the river and water bodies class shown in Figs. 9 and 10. Performance shown in the error matrices revealed that their producer's accuracy was 29.4 and 52.3% at 71.0% and 48.0% omission error, respectively. Under the superclass of vegetation, it is observed from Figs. 9 and 10 that pixels of agricultural crops and natural vegetation are poorly separated and approximately 92% pixels of natural vegetation were wrongly attributed as agriculture. Resultantly, the overall poor agreement between classified and real-world landscape was recorded because kappa, k , was also very low, 0.52.

The overall classification accuracy of unsupervised classification with medium-resolution pan-sharpened imagery (55.4%) was slightly better than composite imagery of Landsat OLI sensor (54.9%) but collectively smaller than that of high-resolution imagery of RapidEye (57.0%). Insight into the error matrix of sharpened and non-sharpened composite imagery of Landsat OLI sensor is shown in Tables 7 and 8. It was ascertained that inter-class and intra-class overlapping of pixels has substantially lowered the classification accuracy of Landsat OLI imagery. In classified raster data of the Landsat OLI sensor, water bodies were separated at zero commission error but producer's accuracy was 76.2% due to the wrongful addition of 23% of pixels of river and seawater classes as shown in Figs. 9 and 10. The pixels of bare soil were also scattered and wrongly counted into wet soil/wetlands, local settlement, agriculture, natural vegetation and canal classes due to which its producer's accuracy was 14.3 with 74.3% commission error. Similarly, pixels of seawater, canals and bare soil were incorrectly cast into local

Table 6 Error matrix of RapidEye image using unsupervised classification

Class	Reference data													Row total	Producer's accuracy	User's accuracy	Commission error	Omission error	
	Water bodies	River	Seawater	Canal	Sand bars	Bare soil	Wetlands	Local settlements	Agriculture	Natural vegetation									
Water bodies	11													11	52.38	100	0	0.48	
River		5		5										10	29.41	50	50	0.71	
Seawater	10	12	12											34	100	35.29	0	0	
Canal				10		2								12	66.67	83.34	16.67	0	
Sand bars					15		10							33	100	45.46	54.55	0	
Bare soil					4	1	12							17	23.53	23.53	76.47	0.29	
Wetlands						12	1							13	80	92.31	7.69	0	
Local settlements					5		13							18	35.14	72.23	0	0.03	
Agriculture										22				34	100	64.71	35.29	0	
Natural vegetation							1				22			2	7.70	50	50	1	
Column total	21	17	12	15	15	17	37	22	13	22	15	15	184						
Overall classification accuracy																			57%
Kappa coefficient, K																			0.52

Table 8 Error matrix of Landsat pan-sharpened image using unsupervised classification

Class	Reference data													Row total	Producer's accuracy	User's accuracy	Commission error	Omission error	
	Water bodies	River	Seawater	Canal	Sand bars	Bare Soil	Wetlands	Local settlements	Agriculture	Natural vegetation									
Water bodies	20	14	7	2									43	95.24	46.51	53.49	0.047		
River		2	1	2		1							6	11.77	33.34	66.67	0.058		
Seawater	1	1	3										5	25.00	60.00	0	0.083		
Canal				3									3	20.00	100	0	0.533		
Sand bars					15	5							20	100	75.00	25.00	0		
Bare soil				1	10	10	27	2					40	58.84	25.00	72.50	0.117		
Wetlands			1	5		14							20	93.34	70.00	0	0		
Local settlements						2	8						10	21.62	80.00	0	0.054		
Agriculture								20					26	90.91	76.92	23.077	0		
Natural vegetation				2			2		6				11	53.85	63.64	63.64	7		
Column total	21	17	12	15	15	17	37	22	13	184									
Overall classification accuracy																			
Kappa coefficient, K																			

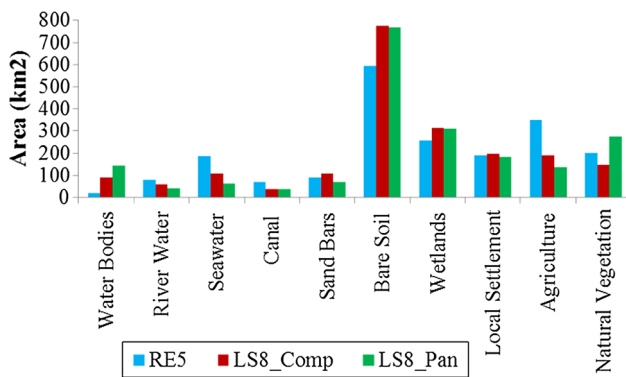


Fig. 7 Visual comparison of area distribution in ten classes with unsupervised classification using RapidEye (5 m), Landsat (30 m) and Landsat (15 m) pan-sharpened, respectively

settlement class and its producer's accuracy was 35.1%. A major proportion of natural vegetation was wrongly falling in agriculture class due to which its producer's accuracy was 30.8 at 80.0% commission error.

Nevertheless, the mingling of inter- and intra-class pixels was also observed in the classified image of pan-sharpened imagery of the OLI sensor. Quantitative analysis is undertaken in Table 8 which exhibits that pixels of the river, seawater and the canal class were closely overlapping with a water bodies class which is why their producer's accuracy remained 95.2, 11.8, 25.0 and 20.0%, respectively. The majority of pixels of the local settlement class were incorrectly falling into the bare soil class. This classification method was a poor separator of natural vegetation from agriculture, and a notable proportion of this class overlapped with canal and local settlements. Due to the larger overlapping of class to class and within individual class, the reliability of this classification method was poor with a kappa coefficient of 0.50.

3.2.3 Supervised Classification

The raster image was classified by feeding the training samples into the maximum likelihood algorithm for supervised classification. On the basis of training samples, area calculated for each remotely sensed product is shown Fig. 8. The area-based quantitative analysis of supervised classification reveals that Landsat OLI imagery and its pan-sharpened image gave pretty close results for water bodies, seawater, sand bars, wet soil/wetland and agriculture classes. However, the area occupied by the river and local settlement classes was calculated higher in RapidEye imagery than both types of Landsat OLI sensor but this proportion got reversed in the canal, bare soil and natural vegetation classes when results of area computation of Landsat OLI sensor were higher than RapidEye imagery.

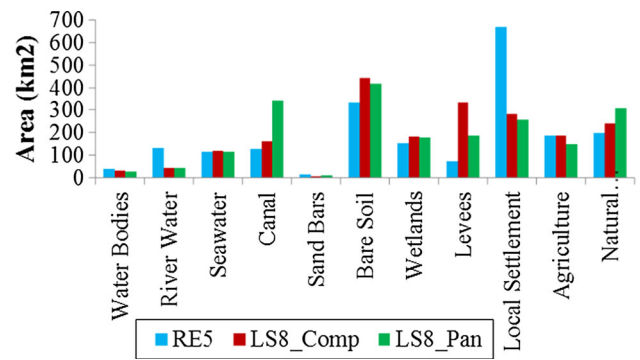


Fig. 8 Visual comparison of area distribution in eleven classes with supervised classification using RapidEye (5 m), Landsat (30 m) and Landsat (15 m) pan-sharpened, respectively

Individual class-based accuracy is tabulated in Tables 9, 10 and 11. Overall classification accuracy for RapidEye, Landsat-8 composite and Landsat-8 pan-sharpened were 79.9, 90.2 and 89.7%, respectively. RapidEye imagery performed well for the separation of water bodies from natural vegetation and showed better producers' accuracy and lower omission errors. The lowest performance of this fine-resolution product, in terms of producer's accuracy, was observed in local settlements and the levee class that was 50.0 and 47.6%, respectively. An in-depth examination of Table 6 for the reasons behind the lower accuracy has exposed that supervised classification over fine-resolution imagery could not successfully separate the mixed pixel of local settlements, bare soil and levee classes, which is why a poor agreement between real and classified points was measured as kappa, k , coefficient 0.77. Visual verification of these findings is depicted in clip 1 (Figs. 9, 10) where right levee has clearly confused its pixels with local settlement pixels, but water bodies, river and natural vegetation were extracted in a satisfactory way. However, supervised classification was successful to separate the sand bars at 100% accuracy with zero error in all remotely sensed images.

Furthermore, the accuracy of the pan-sharpened image was closely equal to that of the composite image of Landsat OLI sensor, but the highest kappa coefficient, 0.89, was computed for the later image because it had a lower error in the separation of the canal, bare soil and local settlement classes. *Spatial Interpretation.* The visual interpretation of high-resolution imagery resulted in a fairly good recognition of land use cover as also reported by Munechika et al. [30]. Water bodies of all sizes and stream channels up to 10 m top-width, but not lower, were detectable. However, through automatic classification technique channels having a top-width of up to 15 m were detectable but lower than that it was not possible due to the overlapping of water class pixels with wet soil/wetland. Similarly, the pan-sharpened image of Landsat OLI was useful for detec-

Table 9 Error matrix of RapidEye image using supervised classification

Class	Reference data													Row total	Producer's accuracy	User's accuracy	Commission error	Omission error
	Water bodies	River	Seawater	Canal	Sand bars	Bare soil	Wetlands	Levees	Local settlements	Agriculture	Natural vegetation							
Water bodies	20	2	2											24	95.24	83.34	16.67	0.226
River	1	15												16	88.24	93.75	0	0
Seawater			10											10	83.34	100	0	0
Canal				15			3							18	100	83.34	16.67	0
Sand bars					15									15	100	100	0	0
Bare soil						13		5	6					24	76.47	54.17	45.84	1.384
Wetlands							12							12	80.00	100	0	0
Levees						3		10	2					15	47.62	66.67	13.34	1.360
Local settlements						1		6	8					15	50.00	53.34	0	0
Agriculture										19		3		22	86.36	86.37	13.64	0.619
Natural vegetation										3	10			13	76.92	76.92	76.93	76.923
Column total	21	17	12	15	15	17	15	21	16	22	13			184				
Overall classification accuracy															79.89%			
Kappa coefficient, K															0.77			

Table 10 Error matrix of Landsat composite image using supervised classification

Class	Reference data													Row total	Producer's accuracy	User's accuracy	Commission error	Omission error	
	Water bodies	River	Seawater	Canal	Sand bars	Bare soil	Wetlands	Levees	Local settlements	Agriculture	Natural vegetation								
Water bodies	19	2												21	90.48	90.48	9.52	0.45	
River	1	15												16	88.24	93.75	0.00	0.00	
Seawater			11											11	91.67	100.00	0.00	0.69	
Canal	1			15		1					1			18	100.00	83.33	11.11	0.00	
Sand bars					15									15	100.00	100.00	0.00	0.00	
Bare soil		1				1	1	3						23	100.00	73.91	21.74	0.00	
Wetlands							13							13	86.67	100.00	0.00	0.00	
Levees								20			1			22	95.24	90.91	9.09	0.00	
Local settlements									13					14	81.25	92.86	7.14	0.00	
Agriculture										20				23	90.91	86.96	13.04	0.00	
Natural vegetation											8			8	61.54	100.00	100.00	61.54	
Column total	21	17	12	15	15	17	15	16	22	22	13			184					
Overall classification accuracy																			90.21%
Kappa coefficient, K																			0.89

Table 11 Error matrix of Landsat pan-sharpened image using supervised classification

Class	Reference data													Row total	Producer's accuracy	User's accuracy	Commission error	Omission error
	Water bodies	River	Seawater	Canal	Sand bars	Bare soil	Wetlands	Levees	Local settlements	Agriculture	Natural vegetation							
Water bodies	20	1	1										22	95.24	90.91	9.09	0.23	
River		16											16	94.12	100.00	0.00	0.00	
Seawater			10			1							11	83.33	90.91	9.09	0.69	
Canal	1			15						2			18	100.00	83.33	11.11	0.00	
Sand bars					15								15	100.00	100.00	0.00	0.00	
Bare soil			1			17	4	2					25	100.00	68.00	28.00	0.00	
Wetlands							13						13	86.67	100.00	0.00	0.00	
Levees								16	1	1			18	76.19	88.89	11.11	0.23	
Local settlements								1	13				14	81.25	92.86	0.00	0.00	
Agriculture										20			21	90.91	95.24	4.76	0.21	
Natural vegetation										1			11	76.92	90.91	90.91	76.92	
Column total	21	17	12	15	15	17	15	21	16	22	13	184						
Overall classification accuracy																		89.67%
Kappa coefficient, K																		0.88

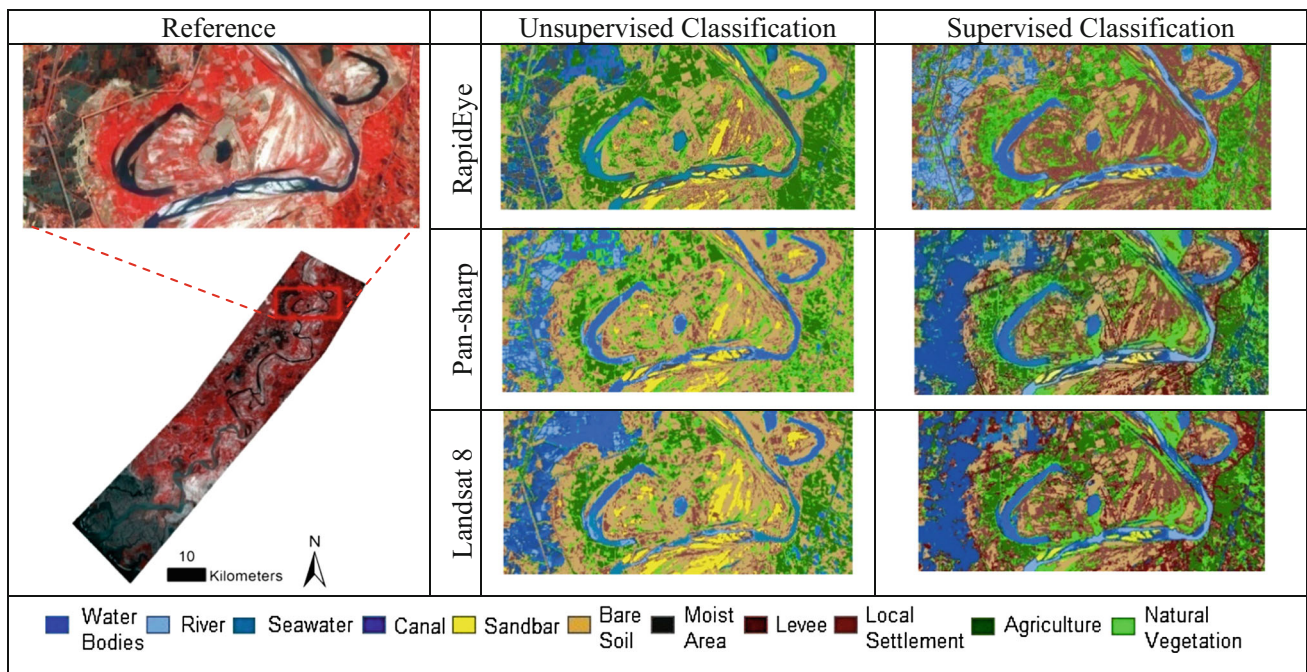


Fig. 9 Visual comparison of classified images of study area (shown in clip 1)

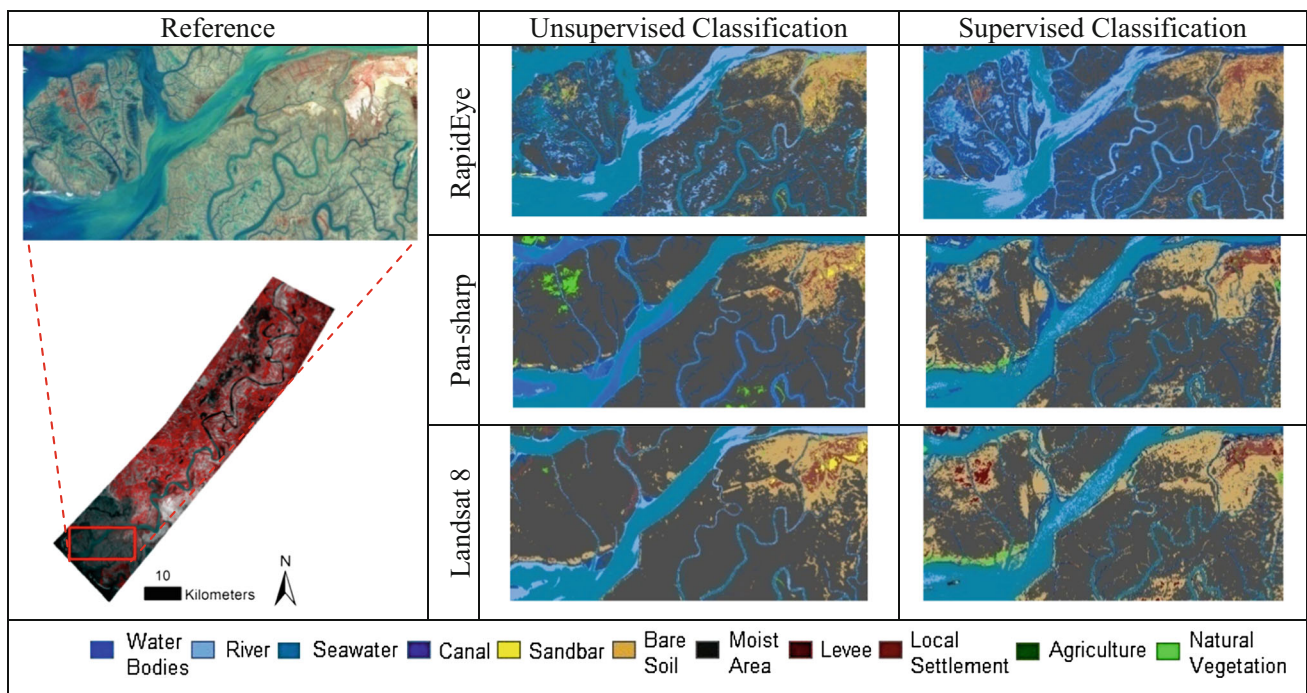


Fig. 10 Visual comparison of classified images of study area (shown in clip 2)

tion of channels with top-width more than 20m and it was cross-checked over incising tidal channels existing on the right and left side of the river mouth in clip 2 of Figs. 9 and 10 [15]. On medium resolution, narrow branches of tidal channels were misclassified due to non-dissociation of the pixel size of 15 and 30m of the Landsat OLI sensor

[15]. Natural vegetation and agricultural fields as small as of 10 m width, trees and shrubs along canals and main river and even in floodplains were detected using high-resolution imagery of the RapidEye sensor, while OLI imagery of Landsat could not dissociate them due to the issue of pixel size.

It was also observed that the reliability of classification techniques was compromised due to the pixel size in the imagery that was not compatible with targeted ground features and resultantly false positives occurred. A detailed review by [8] addressed a similar issue and asserted that pixel sizes smaller than the targeted class in the fluvial environment can even lead to poor delimitation due to the closed reflectance of adjacent pixels of water, sand or vegetation [8]. *Spectral Interpretation.* The use of multispectral imagery enables to distinguish land features of close spectral signatures. Narrowing the spectral bandwidth leads to the extraction of rich information of land use on the ground [31]. Therefore, a spectral comparison given in Table 1 indicates that OLI imagery of Landsat-8 ranges from 430 to 2290 nm, while multispectral RapidEye imagery ranges from 440 to 850 nm. Spectral reflectance of vegetation in the visible range was poor, while stronger in the infrared portion which is why three IR bands of OLI as compared with single IR band of RapidEye resulted in a higher classification accuracy [32]. Despite the spatial difference, the spectral resolution of the first seven bands of the OLI sensor confirmed its suitability for detection of river geomorphology and adjoining ecologic features were determined [33]. The spatial trend of variation in the spectral response of the water class as shown in Table 3 was predominantly due to change in biological as well as physiochemical characteristics of water and its corresponding depth.

The significance of visual interpretation for analysis of remotely sensed imagery prevails, and the high spatial resolution is more suitable due to improved signal-to-background-interference ratio for detection of small targets [7]. Similarly, visual inspection enabled to recognize the riverine features based on their spatial arrangement and ease in translation of its contextual information. Semi-automatic classifications' performance using high spatial resolution was less than medium-resolution imagery of Landsat that was also reported by various researchers [31, 33–38]. Prima facie, there is the likelihood that it occurred because of the spatial sensitivity of high resolution toward boundaries of contiguous landscapes and poor separability due to the limited spectral range. A detailed discussion on implications of the use of high spatial resolution and its subsequent effects on internal variability of homogeneous spectral footprints of land cover and an ultimate decrease in classification accuracy is also reported in different studies [39–41].

A thorough examination of classified clips of high-resolution imagery in Figs. 9 and 10 along with Tables 6 and 9 was made in order to track the subtle differences which revealed moist patches or shady areas along the canal, which were confused as wet soil/wetland because electromagnetic reflectance of moist soil reduces the spectral response and becomes the same as that of wet areas,

and identical findings have been reported by Dare and Liu et al [40, 41]. Similarly, there were major intra-class misclassifications in the superclass land, especially sand bars, bare land, local settlement and levees due to the contiguous spectral signature. Therefore, the superclass land may be delimited for a more distinctive separation of its subordinate classes either by masking all the classes other than land and then performing the same classification or by the use of the thermal infrared bands 10 and 11 of Landsat-8 [42].

4 Conclusions

In the present study, the application of visual, single-band density slicing and multispectral semi-automatic algorithms was tested over multiple spatial resolution imageries. All infrared bands performed considerably better in density slicing than visible bands of Landsat OLI sensor. Importantly, shortwave infrared-2 (band 7) distinguished water from non-water pixels well with density slicing showing the highest overall producer's accuracy of 89% and zero commission error but 34% commission error due to the addition of non-water pixels (predominantly moist/wet soil and water channels <20 m top-width).

The spectral response of composite image of the Landsat OLI sensor proved to be a reliable mean for extraction of riverine landforms and monitoring of its hydromorphologic features in terms of sand dunes, point bars, oxbow lakes, lagoons and relic channels along with meandering bends of the Indus River in the deltaic plain of Pakistan. Analytical and statistical comparisons of semi-automatic classification techniques have substantiated that supervised classification using the maximum likelihood algorithm is an accepted and reliable technique for the extraction of riverine landforms with an overall accuracy of 90.2% and it may be further used for temporal analysis. Results using RapidEye imagery were relatively lower which did not cast any offset because rapidly varying water balance in the lower oceanic portion of the study area and the subsequent submergence of mudflats caused variation in the reflectance of bare soil adjacent to sea-intruded areas which could be an acceptable reason. All classes of water, land and vegetation superclasses were automatically detected in compliance with the visual interpretation of reference points with nominal inter- and intra-class overlapping. It could be maintained that spectral resolution along with close similarity of acquisition time matters more than spatial resolution for delineation of morphologic features of such estuarine reaches. Thus, it is recommended that the optimum combination of spatial and spectral resolutions may be formulated with a medium and high resolution of remotely sensed data for this study area.

Acknowledgements The authors would like to exclusively acknowledge Dr. Jan Dempewolf, Assistant Research Professor, Department of Geography, University of Maryland, USA, for technical and grammatical review. Moreover, the United States Geological Survey (USGS) and Google Earth are also acknowledged who have voluntarily offered satellite data online for research facilitation.

Conflict of interest The authors declare no conflict of interests.

References

- Hazarika, N.; Das, A.K.; Borah, S.B.: Assessing land-use changes driven by river dynamics in chronically flood affected Upper Brahmaputra plains, India, using RS-GIS techniques. *Egypt. J. Remote Sens. Space Sci.* **18**(1), 107–118 (2015)
- Jagers, H.R.A.: *Modelling Planform Changes of Braided Rivers*. University of Twente, Enschede (2003)
- Gilvear, D.; Bryant, R.: Analysis of aerial photography and other remotely sensed data. *Red* **600**(5.8), 23 (2003)
- Goetz, S.J.; Gardiner, N.; Viers, J.H.: Monitoring freshwater, estuarine and near-shore benthic ecosystems with multi-sensor remote sensing: an introduction to the special issue. *Remote Sens. Environ.* **112**(11), 3993–3995 (2008)
- Leuven, R.S.E.W.; Poudevigne, I.; Teeuw, R.M.: *Application of Geographic Information Systems and Remote Sensing in River Studies*. Backhuys Publishers, Leiden, The Netherlands (2002)
- Okin, G.S.; Roberts, D.A.; Murray, B.; Okin, W.J.: Practical limits on hyperspectral vegetation discrimination in arid and semiarid environments. *Remote Sens. Environ.* **77**(2), 212–225 (2001)
- Shaw, G.A.; Burke, H.H.K.: Spectral imaging for remote sensing. *Linc. Lab. J.* **14**(1), 3–28 (2003)
- Gilvear, D.J.; Bryant, R.; Hardy, T.: Remote sensing of channel morphology and in-stream fluvial processes. *Prog. Environ. Sci.* **1**, 257–284 (1999)
- Giri, C.; Long, J.; Abbas, S.; Murali, R.M.; Qamer, F.M.; Pengra, B.; Thau, D.: Distribution and dynamics of mangrove forests of South Asia. *J. Environ. Manag.* **148**, 101–111 (2015)
- Johnston, R.M.; Barson, M.M.: Remote sensing of Australian wetlands: an evaluation of Landsat TM data for inventory and classification. *Mar. Freshw. Res.* **44**(2), 235–252 (1993)
- Frazier, P.S.; Page, K.J.: Water body detection and delineation with Landsat TM data. *Photogramm. Eng. Remote Sens.* **66**(12), 1461–1468 (2000)
- Gilvear, D.J.; Davids, C.; Tyler, A.N.: The use of remotely sensed data to detect channel hydromorphology; River Tummel, Scotland. *River Res. Appl.* **20**(7), 795–811 (2004)
- Du, Z.; Li, W.; Zhou, D.; Tian, L.; Ling, F.; Wang, H.; Sun, B.: Analysis of Landsat-8 OLI imagery for land surface water mapping. *Remote Sens. Lett.* **5**(7), 672–681 (2014)
- Isikdogan, F.; Bovik, A.; Passalacqua, P.: Automatic channel network extraction from remotely sensed images by singularity analysis. *IEEE Geosci. Remote Sens. Lett.* **12**(11), 2218–2221 (2015)
- Donchyts, G.; Schellekens, J.; Winsemius, H.; Eisemann, E.; van de Giesen, N.: A 30 m resolution surface water mask including estimation of positional and thematic differences using landsat 8, srtm and openstreetmap: a case study in the Murray-Darling Basin, Australia. *Remote Sens.* **8**(5), 386 (2016)
- Khan, T.M.A.; Razaq, D.A.; Chaudhry, Q.U.Z.; Quadri, D.A.; Kabir, A.; Sarker, M.A.: Sea level variations and geomorphological changes in the coastal belt of Pakistan. *Mar. Geod.* **25**(1–2), 159–174 (2002)
- Siddiqui, M.N.; Jamil, Z.; Afsar, J.: Monitoring changes in riverine forests of Sindh-Pakistan using remote sensing and GIS techniques. *Adv. Space Res.* **33**(3), 333–337 (2004)
- Qamer, F.M.; Ashraf, M.S.; Hussain, N.; Saleem, R.; Ali, H.; Mirza, H.; Raza, S.M.: Pakistan Wetlands GIS—a multi-scale national wetlands inventory. In: 33rd International Symposium on Remote Sensing of Environment (2008)
- Syvitski, J.P.; Overeem, I.; Brakenridge, G.R.; Hannon, M.: Floods, floodplains, delta plains—a satellite imaging approach. *Sed. Geol.* **267**, 1–14 (2012)
- Mahar, G.A.; Zaigham, N.A.: Examining spatio-temporal change detection in the Indus river delta with the help of satellite data. *Arab. J. Sci. Eng.* **40**(7), 1933–1946 (2015)
- Gilvear, D.; Tyler, A.; Davids, C.: Detection of estuarine and tidal river hydromorphology using hyper-spectral and LiDAR data: forth estuary, Scotland. *Estuar. Coast. Shelf Sci.* **61**(3), 379–392 (2004)
- Kalhor, N.A.; Saleem, M.; Muhammad, F.; Bhutto, A.H.: Dynamics of a polluted Tidal Estuary, Gizri Creek during south west monsoon. *Sch. Acad. J. Biosci.* **3**(1A), 46–51 (2015)
- Ouma, Y.O.; Tateishi, R.: A water index for rapid mapping of shoreline changes of five East African Rift Valley lakes: an empirical analysis using Landsat TM and ETM+ data. *Int. J. Remote Sens.* **27**(15), 3153–3181 (2006)
- Ji, L.; Geng, X.; Sun, K.; Zhao, Y.; Gong, P.: Target detection method for water mapping using landsat 8 OLI/TIRS imagery. *Water* **7**(2), 794–817 (2015)
- Klemenjak, S.; Waske, B.; Valero, S.; Chanussot, J.: Automatic detection of rivers in high-resolution SAR data. *IEEE J. Sel. Top. Appl. Earth Obs. Remote Sens.* **5**(5), 1364–1372 (2012)
- Tapsall, B.; Milenov, P.; Tasdemir, K.: Analysis of RapidEye imagery for annual landcover mapping as an aid to European Union (EU) Common Agricultural Policy. In: Wagner, W., Szekely, B. (eds.) *ISPRS TC VII Symposium 100 Years ISPRS, Vienna, Austria, 5-7 July, Vienna, Austria, vol. 38, part 7B*, pp. 586–573. The International Archives of the Photogrammetry, Remote Sensing and Spatial Information Sciences (2010)
- Yao, F.; Wang, C.; Dong, D.; Luo, J.; Shen, Z.; Yang, K.: High-resolution mapping of urban surface water using ZY-3 multi-spectral imagery. *Remote Sens.* **7**(9), 12336–12355 (2015)
- Banko, G.: A Review of Assessing the Accuracy of Classifications of Remotely Sensed Data and of Methods including Remote Sensing Data in Forest Inventory. International Institute for Applied Systems Analysis, Laxenburg (1998)
- Jensen, J.R.: *Introductory Digital Image Processing: A Remote Sensing Perspective*. Univ. of South Carolina, Columbia (1986)
- Munehchika, C.K.; Warnick, J.S.; Salvaggio, C.; Schott, J.R.: Resolution enhancement of multispectral image data to improve classification accuracy. *Photogramm. Eng. Remote Sens.* **59**(1), 67–72 (1993)
- Gao, J.: A comparative study on spatial and spectral resolutions of satellite data in mapping mangrove forests. *Int. J. Remote Sens.* **20**(14), 2823–2833 (1999)
- Purkis, S.J.; Klemas, V.V.: *Remote Sensing and Global Environmental Change*. Wiley, New York (2011)
- Green, E.P.; Clark, C.D.; Mumby, P.J.; Edwards, A.J.; Ellis, A.C.: Remote sensing techniques for mangrove mapping. *Int. J. Remote Sens.* **19**(5), 935–956 (1998)
- Lee, T.M.; Yeh, H.C.: Applying remote sensing techniques to monitor shifting wetland vegetation: a case study of Danshui River estuary mangrove communities, Taiwan. *Ecol. Eng.* **35**(4), 487–496 (2009)
- Lu, D.; Batistella, M.; Moran, E.; de Miranda, E.E.: A comparative study of Landsat TM and SPOT HRG images for vegetation classification in the Brazilian Amazon. *Photogramm. Eng. Remote Sens.* **74**(3), 311–321 (2008)
- Mahavir, : High (spatial) resolution vs. low resolution images : a planner's view point. *Photogramm. Eng. Remote Sens.* **33**(B7), 6 (2000)



37. Ridd, M.K.: Exploring a VIS (vegetation-impervious surface-soil) model for urban ecosystem analysis through remote sensing: comparative anatomy for cities†. *Int. J. Remote Sens.* **16**(12), 2165–2185 (1995)
38. Takara, K.; Kojima, T.: GIS-aided land cover classification assessment based on remote sensing images with different spatial resolutions. *IAHS Publ. Ser. Proc. Rep. Intern Assoc Hydrol. Sci.* **235**, 659–668 (1996)
39. Carleer, A.P.; Debeir, O.; Wolff, E.: Assessment of very high spatial resolution satellite image segmentations. *Photogramm. Eng. Remote Sens.* **71**(11), 1285–1294 (2005)
40. Dare, P.M.: Shadow analysis in high-resolution satellite imagery of urban areas. *Photogramm. Eng. Remote Sens.* **71**(2), 169–177 (2005)
41. Liu, Z.; Yao, Z.; Wang, R.: Assessing methods of identifying open water bodies using Landsat 8 OLI imagery. *Environ. Earth Sci.* **75**(10), 1–13 (2016)
42. Breunig, F.M.; Galvão, L.S.; Formaggio, A.R.: Detection of sandy soil surfaces using ASTER-derived reflectance, emissivity and elevation data: potential for the identification of land degradation. *Int. J. Remote Sens.* **29**(6), 1833–1840 (2008)

